The Design and Implementation of COSEM, an Iterative Algorithm for Fully 3-D Listmode Data

Ron Levkovitz, Dmitry Falikman*, Michael Zibulevsky, Aharon Ben-Tal, and Arkadi Nemirovski

***Abstract*—In this paper,we present coincidence-list-ordered sets expectation-maximization (COSEM), an algorithm for iterative image reconstruction directly from list-mode coincidence acquisition data. The COSEM algorithm is based on the ordered sets EM algorithm for binned data but has several extensions that makes it suitable for rotating two planar detector tomographs. We develop the COSEM algorithm and extend it to include analytic calculation of detection probability, noise reducing iterative filtering schemes, and on-the-fly attenuation correction methods. We present an adaptation of COSEM to the Varicam\VG camera and show results from clinical and phantom studies.**

***Index Terms*—3-D reconstruction, expectation maximization, iterative algorithms, PET.**

I. Introduction

THE MAXIMUM-likelihood expectation-maximization (ML-EM) iterative reconstruction algorithm [9] is considered as a "golden standard" in medical image reconstruction; its high computational demands, however, prevented it from being widely accepted for industrial and clinical use. In 1994, Hudson and Larkin [5] presented an accelerated version of the EM algorithm based on an ordered sets approach. Many independent tests have shown that the ordered-sets EM (OSEM) produces images which are similar in quality to those produced by the EM algorithm in a fraction of the time [4], [7]. The OSEM and the EM algorithms use binned data (e.g., projection sets) to reconstruct the image. This poses a severe limitation on the utilization of OSEM for reconstructions of three-dimensional (3-D) acquisition images from scanners with wide axial apertures, high resolution and low statistics. These scanners are characterized by a huge number of bins (hundreds of millions) and relatively small data sets. The resulting projection set will be huge, and mostly empty.

Scanners with wide axial apertures, such as revolving two-head gamma camera scanner or positron emission tomography (PET) with large numbers of rings, typically produce data in list mode format. List-mode data format is an event by event account of the acquisition process. The events are, therefore, ordered according to the time of acquisition. Standard reconstruction methods bin these events to sinograms and use the conventional reconstruction techniques. In this paper, we develop a coincidence-list-ordered sets expectation-maximization (COSEM) algorithm. The COSEM algorithm is a full 3-D algorithm, particularly suited for large axial aperture tomographs. It avoids the binning problem by directly processing the coincidence list information. The direct processing of the time-based coincidence list instead of the geometric-based ordered sets used by the standard OSEM provides a natural framework for evolving images and dynamic reconstruction. This algorithm is similar in approach to the algorithms independently developed by Barret *et al.* [1] and Reader *et al.* [10]. A purely theoretical algorithm is presented in [1]. An implementation and further development of the algorithm presented in [1] is described in [2], but it is still far from being implemented for real clinical studies. In contrast, COSEM includes many features (correction factors, exact probability calculation, iterative Metz and Gaussian filtering schemes), is clinically approved and is now in routine clinical use.

Manuscript received January 8, 1999; revised April 14, 2001. This work was supported in part by the European Commission PARAPET ESPRIT Project, in part by the Israeli Ministry of Science, and in part by ELGEMS LTD. The Associate Editor responsible for coordinating the review of this paper and recommending its publication was C. Thompson. *Asterisk indicates corresponding author.*

R. Levkovitz, M. Zibulevsky, and A. Nemirovski are with the Minerva Optimization Centre, Technion, Haifa 32000, Israel.

*D. Falikman is with the Minerva Optimization Centre, Technion, Haifa 32000, Israel (e-mail: dmfalikman@ie.technion.ac.il).

A. Ben-Tal is with the ITS Faculty, Department of Control, Risk, Operations Research and Statistics, Technical University of Delft, 2628CD Delft, The Netherlands.

Publisher Item Identifier S 0278-0062(01)05522-7.

II. The Mathematical Model

A. The EM Algorithm

Consider a body with a variable radiation density contained in the discretized cube $B(x, y, z)$. Let $\lambda(v)$ denote the emission density of each unit box (voxel) $v = (x, y, z)$ in the cube. The radiation emitted by the body (pairs of photons produced by the corresponding positron–electron annihilations) is detected by the encircling detectors. If two photons are "simultaneously" detected by two detectors and if the line of response (LOR), defined by the two sets of detection coordinates, intersects the body, we consider this as a coincidence acquisition (event). In essence, all coincidence acquisition reconstruction algorithms try to determine the unknown activity distribution in the cube given the list of detected events.

The PET scanner is built of rows of detector rings whereby each detector is regarded as a discrete unit. All the events detected simultaneously by the same two detectors d_i and d_j are collected in the single bin b_{ij}. Thus, each bin b defines a single LOR (a tube, in fact) and every event detected in this bin is assumed to have originated along this LOR.

Let $v = 1, \ldots, V$ represent the voxels of the field of view (FOV) cube and let independent Poisson variables with unknown means $\lambda(v)$ represent the number of unknown observed emissions in each of the V voxels. Suppose that an

emission from the voxel v is detected in bin b with probability $p(v, b)$, $b = 1, \ldots, B$. The transition matrix $p(v, b)$ (likelihood matrix) is assumed known. We observe the total number $y = y(b)$ of events detected by each bin b and wish to estimate the unknown $\lambda = \lambda(v)$, $v = 1, \ldots, V$. For each λ, the observed data y has the conditional probability (likelihood)

$$P(y|\lambda) = \prod_{1 \le b \le B} e^{-\mu(b)} \frac{\mu(b)^{y(b)}}{y(b)!} \tag{1}$$

where $\mu(b)$ is the mean of the Poisson variable $y(b)$, that is

$$\mu(b) = \sum_{1 \le v \le V} \lambda(v) p(v, b). \tag{2}$$

The ML estimate of λ is

$$\overline{\lambda} = \arg\max_{\lambda} P(y|\lambda). \tag{3}$$

For numerical calculations it is more convenient to work with the *log-likelihood function*

$$\begin{aligned} L(\lambda) &= \ln(P(y|\lambda) \\ &= -\sum_b \mu_b + \sum_b y_b \ln \mu_b + C \end{aligned} \tag{4}$$

where C is a constant which does not affect maximization. The optimality conditions for $\lambda = \lambda(v)$ to achieve the maximum of (4) are, after simple some algebraic manipulations [9]

$$\lambda(v) = \frac{1}{P(v)} \sum_{b=1}^{B} \frac{y(b)\lambda(v)p(v, b)}{\sum_{v'=1}^{V} \lambda(v')p(v', b)}, \qquad v = 1, \ldots, V \tag{5}$$

where $P(v)$ is the probability of detecting an event emitted from the voxel v, i.e.,

$$P(v) = \sum_{b=1}^{B} p(v, b). \tag{6}$$

The EM algorithm can be viewed as an iterative algorithm for solving the fixed-point equations (5) and (6)

$$\lambda^{new}(v) = \frac{1}{P(v)} \sum_{b=1}^{B} \frac{y(b)\lambda^{old}(v)p(v, b)}{\sum_{v'=1}^{V} \lambda^{old}(v')p(v', b)}, \quad v = 1, \ldots, V. \tag{7}$$

B. The Ordered Sets EM (OSEM) Using Projection Bins

The OSEM algorithm [5] is a relatively straightforward modification of the conventional EM in (7). The projection data are grouped into m subsets, denoted by $B_1, B_2, \ldots, B_m$. The subsets normally consist of projection views separated by some fixed angle about the object.

In the OSEM algorithm, the log-likelihood fixed point equations are iterated for each of the subsets; using the final result of the previous subset as a starting point.

Therefore, an OSEM subiteration is

$$\lambda_{j+1}^{k}(v) = \frac{1}{P(v)} \sum_{b \in B_j} \frac{y(b)\lambda_j^k(v)p(v, b)}{\sum_{v'=1}^{V} \lambda_j^k(v')p(v', b)}, \quad v = 1, \ldots, V \tag{8}$$

where k is the current outer iteration and B_j the current subset. The last subiteration m in k gives the starting point for the next outer iteration $k+1$: $\lambda_0^{k+1} = \lambda_m^k$. This subiteration procedure is repeated until all subsets have been exhausted. Such a cycle is considered a single iteration of OSEM. The cycle is repeated iteratively until a satisfactory reconstruction is obtained. Usually, 1–6 outer iterations (an outer iteration consists of a single pass on all available data) and 16–32 subiterations/iteration (a single pass on part of the data) are sufficient for a good quality reconstruction.

In this framework, EM is a special case of OSEM where the number of subsets is set to $m = 1$. For the case of noiseless projections, it has been shown that each OSEM estimate, based on a subset of projections, converges as fast toward an ML solution as a full iteration of EM using all projections [5]. In other words, if the projection data are divided into m subsets, then once all projections have been used in a single iteration of OSEM an estimate has been produced which is similar to m iterations of EM. It is this property that gives OSEM considerable acceleration compared with EM. It was found, however, that if the data is divided into too many subsets the results deteriorate as noise increases [5].

C. COSEM: An Ordered Sets EM Algorithm for List-Mode Data

The list-mode data is a list of coincident gamma pairs that are serially stored in the chronological order of their registration. It is possible to consider the sinograms as a dense representation of the registered data and the list mode as a sparse representation of the same data. When the number of registered events is limited (several millions, say), the list mode representation is much more efficient compact than the sinogram representation. This is because the sinogram representation does not depend on the number of recorded events but is fixed according to the geometry of the system and can include hundreds of millions of bins. The sinogram element represents a single bin tube (LOR). If such a tube is infinitely thin then the probability of detecting two events in the same bin is negligible. The values of $y(b)$ in (7) are, in this case, either one or zero, where one denotes that a coincidence was detected in this particular LOR. It is easy to see that in the EM algorithm, when $y(b) = 0$, the whole term vanishes for this bin. Therefore, the EM algorithm becomes

$$\lambda^{k+1}(v) = \frac{1}{P(v)} \sum_{b \in B,\, y_b = 1} \frac{\lambda^k(v)p(v, b)}{\sum_{v'=1}^{V} \lambda^k(v')p(v', b)}, \quad v = 1, \ldots, V. \tag{9}$$

In the COSEM algorithm, the above assumption is used. The bins "thickness" is determined according to the detection reso-

lution and, therefore, there is no further rebinning of data. This allows us to perform the calculation of $p(v, b)$ for each bin "on-the-fly" without compromising computational efficiency. This method has three major advantages:

First, the algorithm uses the exact detection points and does not compromise the accuracy by binning the data. Second, the number of operations is dependent on the number of detected events. Third, there is no need to hold the (very large) four-dimensional sinogram representation required for true 3-D reconstruction using binned data.

The extension of (9) to ordered sets is straightforward and natural whereby a subset is made of groups of events in the list-mode data. Such a group represents, for example, acquisition along during a certain period of time, randomly selected events, events acquired at certain angles, etc. Let B be the list of events and let us split B into m sequential sets $B_1, \ldots, B_m$. The COSEM algorithm parallel similar to (8) is

$$\lambda_{j+1}^k(v) = \frac{1}{P(v)} \sum_{b \in B_j,\, y_b = 1} \frac{\lambda_j^k(v) p(v, b)}{\sum_{v'=1}^{V} \lambda_j^k(v') p(v', b)} \qquad v = 1, \ldots, V \tag{10}$$

where k is the current outer iteration and B_j the current subset. The last subiteration m in k gives the starting point for the next outer iteration $k+1$: $\lambda_0^{k+1} = \lambda_m^k$.

III. Correction Factors

The successful implementation of reconstruction algorithms requires the correction of observed data, which are distorted due to physical and geometrical phenomena that are the resulting from of factors like the machine geometry, physical properties, and the radiation process, etc. Most phenomena, detector efficiency for example, are normally corrected directly on the projection set (random subtraction, attenuation weight multiplication, smooth low-pass filtering, etc.). Indeed, in many PET scanners, projection data are automatically pre-corrected during the creation of the projection set. In the 3-D acquisition mode of the dual-head scanner, the projection set is not created. Thus, we must correct the influences of these phenomena either on individual LORs or to take them into account when calculating voxel-detection probabilities.

The probability for LOR detection depends on the relative sensitivity of the tomograph's crystals at the actual detection points, on the geometrical probability of detection, on the body attenuation, and on body and crystal scatter. The COSEM implementation described in this paper includes an exact analytical calculation of each voxel's geometrical detection probability. Other phenomena are taken into account as a global weight assigned to the LOR, $w(b)$. A modified iteration scheme of COSEM is, thus

$$\lambda_{j+1}^k(v) = \frac{1}{P(v)} \sum_{b \in B_j,\, y_b = 1} \frac{\lambda_j^k(v) p(v, b) w(b)}{\sum_{v'=1}^{V} \lambda_j^k(v') p(v', b)} \qquad v = 1, \ldots, V. \tag{11}$$

The assigned LOR weight, $w(b)$, is composed of three elements: $w(b) = w_{\text{scatter}} \times w_{\text{pair}} \times w_{\text{atten}}$ where w_{pair} includes necessary corrections such as uniformity, rate-dependent event loss, isotope decay, and washouts

$$w_{\text{atten}} = \left(\exp\left(\sum_v -l_{v,b} \mu_v \right) \right)^{-1} \approx \left(\exp\left(\sum_v -p(v, b) \mu_v \right) \right)^{-1}. \tag{12}$$

w_{atten} represents a weight inversely proportional to the probability of an event to be attenuated by the body. l_v is the intersection length of the LOR and the voxel, and μ_v is the map of registered attenuation coefficients.

w_{scatter} is a weight given to events according to the detected energy windows. This is a simple dual window method to separate scattered events from photopeak events. The scatter weight is currently calculated as: $w_{\text{scatter}} = 1$ when both photons are registered in the high energy windows; $w_{\text{scatter}} = 0.25$ when one of the photons is registered in the high energy window and the other in the Compton energy window; otherwise, $w_{\text{scatter}} = 0$. These values for w_{scatter} where fixed empirically.

Applying corrections to the LOR is an alternative approach to account for the same effects via the probability of detection matrix $P(v)$. It is easily seen that it is simpler and more computationally efficient to correct effects like attenuation via LOR weights. It is equally easy to see that those LORs which will receive the highest weights are of the lowest probability and these are also those most likely to contain a large noise segment component. For example, correcting attenuation effects via the voxel space requires the calculation of the probability of attenuated emission for each voxel. If a projection set exists, then this can be achieved by an operation computationally equivalent to forward and back projection operations. With the absence of projections, this can be done by simulation of emission in all possible directions; such a task can be computationally more demanding than the entire reconstruction process.

We have, therefore, developed a mixed approach whereby the system-dependent corrections are calculated as voxel-detection probabilities while other corrections, mainly body-dependent corrections, are still applied to LORs. $P(v)$ calculation, including the geometric system corrections, is described in the Section iV.

The presence of random coincidences in the data also requires a special treatment. Normally, the random coincidences are subtracted from the projection data set during binning. This method often creates negative values in bins due to Possion statistics count fluctuation and is, therefore, theoretically and practically problematic for algorithms like the EM. In the absence of projections, however, it is impossible to subtract randoms. Instead, we have devised a new method to handle randoms. The random coincidences, measured in a delayed time window, are used to reconstruct an alternative image. Using the property that this image is featureless, it is filtered This image is filtered with a strong low-pass filter and is subtracted from the real image, voxel by voxel.

We also note that a possible method for body scatter correction is to reconstruct the events in the body scattered dominated energy window separately, to later deconvolve the reconstructed image with the appropriate scatter point-spread function (PSF) and to add it to the original image. This approach is not implemented in the version of COSEM described here and will be discussed in a separate paper devoted to noise correction methods.

IV. Calculation of the Voxel Probabilities Matrix $P(v)$

A. Calculation of $P(v)$ for the Dual Head Scanner

A detector in the dual-head scanner is built of two surfaces. The main one is the crystal, typically an *NaI* crystal with thickness ranging from around 9 mm (3/8″) to 25 mm (1″). On top of this crystal it is common to mount a graded absorber, made of several layers of metal, to prevent low-energy photons resulting from Compton scatter in the body or lead X-rays from reaching the crystal.

Assume, for simplicity, that the graded absorber is a single layer one. We can characterize the detector by the following geometrical parameters (see Fig. 1):

$$0 < R_0 < R_1 < R_2, \qquad H > 0, \qquad L > 0$$

where

R_0, R_1, and R_2	distances from the center of rotation to the graded absorber surface, crystal surface, and crystal end, respectively;
H	half the detector size in the axial dimension;
L	half the detector size in the transaxial dimension.

Define for $i = 0, 1$ the two sets

$$P_i^+: \begin{cases} -L \le x \le L \\ R_i \le y \le R_{i+1} \\ -H \le z \le H \end{cases}$$

$$P_i^-: \begin{cases} -L \le x \le L \\ -R_{i+1} \le y \le -R_i \\ -H \le z \le H \end{cases}. \tag{13}$$

The detectors P^+, P^- in Fig. 1 are defined as the union of the graded absorber layer and the crystal layer $P^+ = P_0^+ \cup P_1^+$, $P^- = P_0^- \cup P_1^-$. In other words, if P^σ is a rectangular detector $\sigma \in \{+, -\}$, then P_0^σ is the graded absorber layer and P_1^σ is the detector layer of the two detector plates P^σ. Finally, $P = P^+ \cup P^-$, defines the tomograph as a union of the two rectangular detectors P^+ and P^-.

The graded absorber and crystal are characterized by the physical attenuation constants μ_0, $\mu_1 > 0$. Therefore, these constants also characterize the detector layers P_i^+, P_i^-, $i = 0, 1$.

During acquisition, the tomograph detectors revolve around the central z axis. Denote by f_γ the rotation function around the z axis on angle γ then

$$f_\gamma: (x, y, z) \to (x\cos\gamma - y\sin\gamma, x\sin\gamma + y\cos\gamma, z). \tag{14}$$

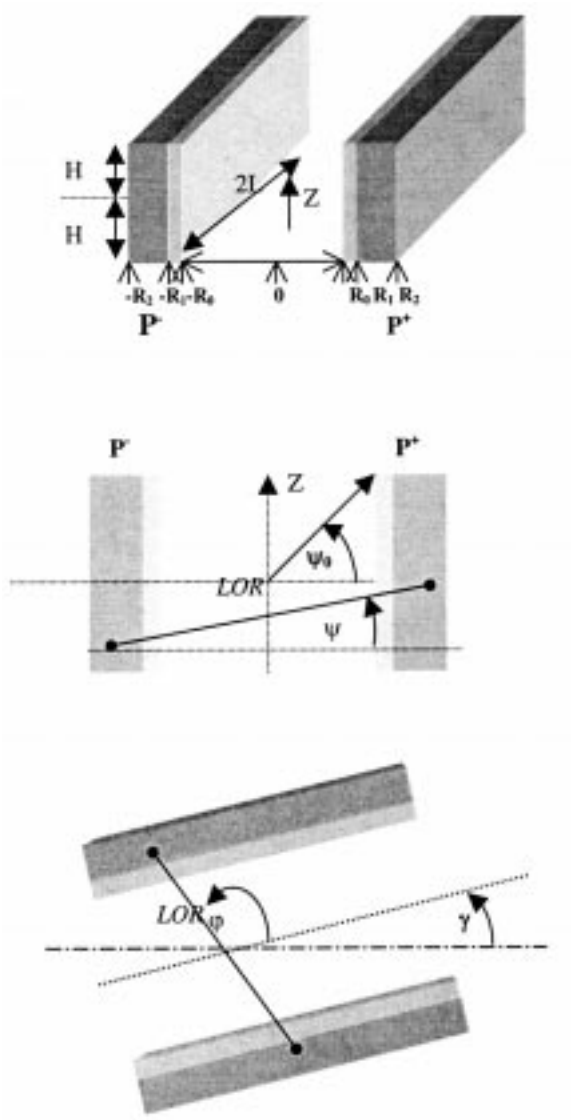

Fig. 1. Dual-head detector system: dimensions and geometry of the revolving system. (top) Dimensions of the system. (middle) LOR emission angles—axial view. (bottom) LOR emission angles—transaxial view.

Equation (14) defines the transformation between a line of the revolving coordinate system attached to the detectors and the standard coordinate system.

Let ψ_0, $0 < \psi_0 < (\pi/2)$ be the maximal axial detection angle of the system. Consider the following subset S_0 of the unit sphere, parameterized by angles (φ, ψ)

$$S_0: \begin{cases} x = \cos\psi\cos\varphi \\ y = \cos\psi\sin\varphi \\ z = \sin\psi \end{cases} : \quad -\pi \le \varphi \le \pi, \ -\psi_0 \le \psi \le \psi_0. \tag{15}$$

Take a point $(r, 0, h)$: $0 \le r < R_0$, $-H < h < H$ and consider a random vector $a = (x, y, z)$, uniformly drawn on S_0, and a random angle γ uniformly drawn on the interval $[-\pi, \pi]$.

Now, consider a LOR of an emission event

$$l = (r, 0, h) + t(x, y, z), \qquad t \in R. \tag{16}$$

The LOR is defined by the point $(r, 0, h)$: $0 \le r < R_0$, $-H < h < H$ and the direction $a = (x, y, z)$. The direction is given in terms of the transaxial and axial emission angles (φ, ψ).

Using equations (13) and (14) consider the image $f_\gamma(P) = f_\gamma(P^+) \cup f_\gamma(P^-)$. $f_\gamma(P^\sigma)$ is the translation of the detector plates P^σ to the standard coordinate system, where γ is the system rotation angle at the time of emission. Using this notation, we can say that the LOR in (16) is detected only if it is detected by both detectors $f_\gamma(P^+)$ and $f_\gamma(P^-)$.

These two detection events are independent and, therefore, the probability that the LOR is detected by $f_\gamma(P)$ is a product of the two events probabilities

$$\text{prob}(l, f_\gamma(P)) = \text{prob}(l, f_\gamma(P^+)) \times \text{prob}(l, f_\gamma(P^-)). \tag{17}$$

The probability to detect the event $\text{prob}(l, f_\gamma(P^\sigma))$, $\sigma \in \{+, -\}$ is dependent on the length of intersection between the LOR l and each detector $f_\gamma(P_i^\sigma)$, l_i^σ

$$\text{prob}(l, f_\gamma(P^\sigma)) = e^{-\mu_0 l_0^\sigma}(1 - e^{-\mu_1 l_1^\sigma}), \qquad \sigma \in \{+, -\}. \tag{18}$$

Let $\text{prob}(l, f_\gamma(P^\sigma)) > 0$ then $l_1^+ > 0$, $l_1^- > 0$ and $l \cap f_\gamma(P_1^+) \neq 0$, $l \cap f_\gamma(P_1^-) \neq 0$ or

$$\begin{aligned} l \cap f_\gamma(P_0^+ \cap P_1^+) &\neq 0 \\ l \cap f_\gamma(P_0^- \cap P_1^-) &\neq 0. \end{aligned} \tag{19}$$

The condition in (19) means that for some numbers $t^+, t^- \in R$:

$$\begin{aligned} (r, 0, h) + at^+ &= f_\gamma(x^+, R_1, z^+) \\ (r, 0, h) + at^- &= f_\gamma(x^-, -R_1, z^-) \end{aligned}$$

where $-L \le x^+, x^- \le L$, $-H \le z^+, z^- \le H$.

Therefore, we have

$$\begin{aligned} f_\gamma^{-1}\{(r, 0, h) + at^+\} &= (x^+, R_1, z^+) \\ f_\gamma^{-1}\{(r, 0, h) + at^-\} &= (x^-, -R_1, z^-). \end{aligned}$$

Let $a = (\cos\psi\cos\varphi, \cos\psi\sin\varphi, \sin\psi)$. From (14) it follows that $f_\gamma^{-1} = f_{-\gamma}$. Hence, after simplification we get

$$\begin{aligned} &\left|r\cos\gamma + t^+\cos\psi\cos(\varphi - \gamma)\right| \le L \\ &\left|r\cos\gamma + t^-\cos\psi\cos(\varphi - \gamma)\right| \le L \\ &t^+\cos\psi\sin(\varphi - \gamma) = R_1 + r\sin\gamma \\ &t^-\cos\psi\sin(\varphi - \gamma) = -R_1 + r\sin\gamma \\ &\left|h + t^+\sin\psi\right| \le H \\ &\left|h + t^-\sin\psi\right| \le H. \end{aligned}$$

This leads to the following system of inequalities, which geometrically defines the detection of the LOR

$$\begin{aligned} &r|\sin\varphi| + R_1|\cos(\varphi - \gamma)| \\ &\quad \le L|\sin(\varphi - \gamma)|, \qquad (20.a) \\ &-\min\left\{\frac{H - h}{R_1 - \xi r\sin\gamma}, \frac{H + h}{R_1 + \xi r\sin\gamma}\right\} \times |\sin(\varphi - \gamma)| \\ &\quad \le \tan\psi \\ &\quad \le \min\left\{\frac{H - h}{R_1 + \xi r\sin\gamma}, \frac{H + h}{R_1 - \xi r\sin\gamma}\right\} \\ &\qquad \times |\sin(\varphi - \gamma)| \qquad (20.b) \end{aligned}$$

where $\xi = \pm 1$ is determined from the condition $\xi\sin(\varphi - \gamma) = |\sin(\varphi - \gamma)|$.

Equation (20.a) gives the transaxial detection condition and (20.b) gives the axial detection conditions for the LOR.

Note that if (19) holds, then $l_0^+ = l_0^- = l_0$

$$l_0 = \frac{R_1 - R_0}{\cos\psi \times |\sin(\varphi - \gamma)|}.$$

Let $p(r, h)$ denote probability that a random line l is detected by the detector $f_\gamma(P)$ for any rotation angle γ, then

$$\begin{aligned} p(r, h) = &\frac{1}{8\pi^2\sin\psi_0} \\ &\cdot \iint\limits_{(\varphi,\gamma)\in G} \left(\int_{\arctan A(\varphi,\gamma)}^{\arctan B(\varphi,\gamma)} \cos\psi e^{-2\mu_0 l_0}(1 - e^{-\mu_1 l_1^+}) \right. \\ &\left. \cdot(1 - e^{-\mu_1 l_1^-})\, d\psi \right) d\varphi\, d\gamma \end{aligned} \tag{21}$$

where

$$G = \left\{ \begin{array}{l} (\varphi, \gamma)\colon -\pi \le \varphi \le \pi,\ -\pi \le \gamma \le \pi, \\ r|\sin\gamma| + R_1|\cos(\varphi - \gamma)| \le \\ L|\sin(\varphi - \gamma)| \end{array} \right\} \tag{22}$$

and

$$\begin{aligned} A(\varphi, \gamma) = &-\min\left\{ \begin{array}{l} \dfrac{H - h}{R_1 - \xi r\sin\gamma}|\sin(\varphi - \gamma)|, \\ \dfrac{H + h}{R_1 + \xi r\sin\gamma}|\sin(\varphi - \gamma)|, \\ \tan\psi_0 \end{array} \right\} \\ B(\varphi, \gamma) = &\min\left\{ \begin{array}{l} \dfrac{H - h}{R_1 + \xi r\sin\gamma}|\sin(\varphi - \gamma)|, \\ \dfrac{H + h}{R_1 - \xi r\sin\gamma}|\sin(\varphi - \gamma)|, \\ \tan\psi_0 \end{array} \right\}. \end{aligned} \tag{23}$$

Equations (22) and (23) are derived from equations (20.a) and (20.b), respectively. Of course, we can replace the point $(r, 0, h)$ with any point (u, v, h) with the property $u^2 + v^2 = r^2$. For this latter point, the corresponding probability is also $p(r, h)$.

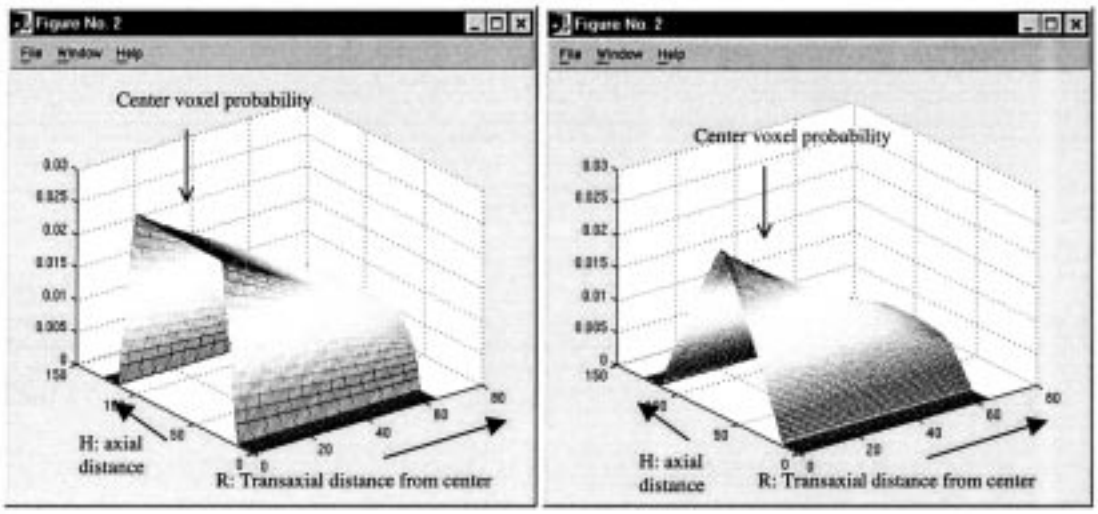

(a) (b)

Fig. 2. Probability matrix $P(v)$ for voxel space 128^3 (normalized values).(a). Full 3-D mode (no septas). (b) Limited 3-D mode (with septas).

The integration domain G and the integrated function are symmetric. Therefore, it is possible to obtain $p(r, h)$ by integrating over a domain G_0 that is eight times smaller than the original domain

$$p(r, h) = \frac{1}{\pi^2 \sin\psi_0} \cdot \iint_{(\varphi,\gamma)\in G_0} \left(\int_{\arctan A_0(\varphi,\gamma)}^{\arctan B_0(\varphi,\gamma)} \cos\psi e^{-2\mu_0 l_0}(1-e^{-\mu_1 l_1^+}) \cdot(1-e^{-\mu_1 l_1^-})\, d\psi \right) d\varphi\, d\gamma \tag{24}$$

where

$$G_0 = \left\{ \begin{array}{l} (\varphi, \gamma)\colon 0 \le \gamma \le \varphi \le \pi, \\ r\sin\varphi + R_1|\cos(\varphi-\gamma)| \\ \le L\sin(\varphi-\gamma) \end{array} \right\} \tag{25}$$

and

$$A_0(\varphi, \gamma) = -\min \left\{ \begin{array}{l} \dfrac{H-h}{R_1 - r\sin\gamma}\sin(\varphi-\gamma), \\ \dfrac{H+h}{R_1 + r\sin\gamma}\sin(\varphi-\gamma), \\ \tan\psi_0 \end{array} \right\}$$

$$B_0(\varphi, \gamma) = \min \left\{ \begin{array}{l} \dfrac{H-h}{R_1 + r\sin\gamma}\sin(\varphi-\gamma), \\ \dfrac{H+h}{R_1 - r\sin\gamma}\sin(\varphi-\gamma), \\ \tan\psi_0 \end{array} \right\}. \tag{26}$$

The only parameter in this last set of equations, (23)–(25), that can change between acquisitions is the rotation radius, R_1 (the distance from the center to the crystal surface). This radius is typically 35 cm for torso and abdomen studies acquisition and 14 cm for brain type acquisition. Fig. 2 illustrates the probability matrix $P(v)$ for torso and abdomen acquisition in limited 3-D and full 3-D acquisition modes.

V. Calculation of $P(v)$ for PET

In conventional PET, we do not have a revolving system but a complete cylinder of detectors. It is common to regard the detection cylinder as a perfect one. In other words, if a LOR intersects the cylinder in on both sides, then it is detected with probability 1. By making the necessary simplifications to the formula in Section IV and by removing the rotation angle γ from the above equations, we obtain the following probability formula:

$$p(r, h) = \frac{1}{\pi} \int_0^{\pi} \frac{d\varphi}{\sqrt{1 + A^2(\varphi)}} \quad 0 \le r \le R_0,\ 0 \le h \le H \tag{27}$$

where $A(\varphi)$ is given in (28), which uses the following scalars:

$$\varphi_0 = \arccos \frac{h\sqrt{R_0^2 - r^2}}{r\sqrt{H^2 - h^2}}, \qquad 0 < \varphi_0 \le \frac{\pi}{2}$$

and

$$t = \sqrt{R_0^2 - r^2\sin^2\varphi}$$

$$A(\varphi) = \left\{ \begin{array}{lll} \dfrac{r\cos\varphi + t}{H+h}, & 0 \le \varphi \le \varphi_0 & \dfrac{h}{H} < \dfrac{r}{R_0} \\ \dfrac{-r\cos\varphi + t}{H-h}, & \varphi_0 < \varphi \le \pi & \dfrac{h}{H} < \dfrac{r}{R_0} \\ \dfrac{-r\cos\varphi + t}{H-h}, & 0 \le \varphi \le \pi & \dfrac{h}{H} \ge \dfrac{r}{R_0}. \end{array} \right. \tag{28}$$

Note that in the case where $r/R > h/H$, φ_0 should be one of the discrete integration points.

The integrals in equations (21) and (27) are computed using the Simpson integration formula. We have found that by dividing the interval $(0, \pi)$ into 100 subintervals we get a sufficient accuracy of 10^{-8}. An illustration of the probability matrix $P(v)$ in the PET case is given in Fig. 3.

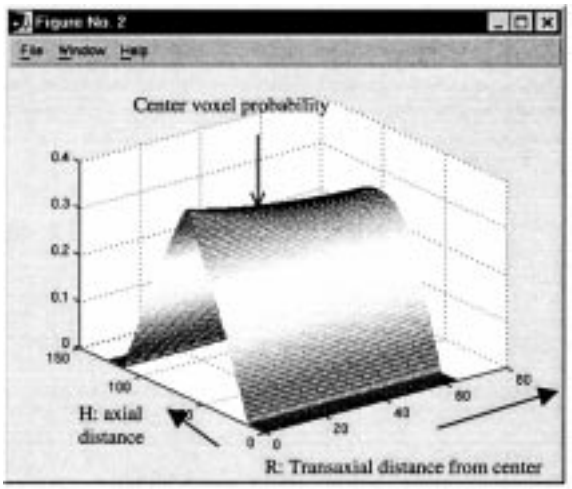

Fig. 3. Probability matrix $P(v)$, PET case, for voxel space 128^3 (normalized values). Full 3-D mode.

VI. Iterative Filtering

It is well known that while the OSEM algorithm progresses from iteration to iteration, the image first improves and then becomes increasingly noisy. This is the result of the algorithm fitting the noise together with the signal. This situation is even more evident in the case of a limited statistics reconstruction where only a fraction of the statistics obtained in a standard PET study is available. Two methods are commonly used to reduce the effect of this problem: postfiltering and Bayesian methods. A Bayesian version of our algorithm is described in [6]. We have found that iterative filtering can also be an effective and efficient way to control noise.

For the purpose of discussing our filtering method, it is convenient to reconsider the EM (OSEM/COSEM) algorithm as series of scaled forward and back projections. Forward projection step

$$\forall b \in B \text{ compute}$$
$$\overline{w(b)} = \sum_v \lambda(v) p(v, b)$$

or

$$\overline{w} = forward\_project(\lambda).$$

Note that $\overline{w}$ represents the observed reading of the density image λ based on the system model encapsulated by the algorithm.

Back projection step

$$\forall v \in V \text{ compute}$$
$$\overline{\lambda(v)} = \sum_b w(b) p(v, b)$$

or

$$\overline{\lambda} = back\_project(w).$$

Using this notation, the COSEM algorithm at the $k+1$ subiteration, [see (11)], can be rewritten as

$$\lambda_j^{k+1} = \frac{\lambda_j^k}{P(v)} back\_project\left(\frac{w}{\overline{w}(\lambda_j^k)^{old}}\right). \quad (29)$$

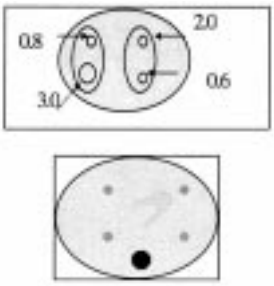

Fig. 4. Phantom designs (top) Phantom 1. (bottom) Phantom 2.

TABLE I
Studies Statistics

		Phantom 1	Phantom 2	Clinical 1
Events in study	Peak	926324	1083291	275818
	Peak/ Compt.	1451160	1746696	400000
	Random	216460	1972837	159230
Acquisition time		48 minutes	30 minutes	30 minutes
Revolutions		16	10	10
Rotation Radius		36.25	37.27	36.75
Background to foreground ratio		16:1	5:1	

While the forward and back projections are performed as before, the new image is the result of convolving the old image with a filtering kernel F before updating it

$$\lambda_j^{k+1} = \frac{F \otimes \lambda_j^k}{P(v)} back\_project\left(\frac{w}{\overline{w}(\lambda_j^k)^{old}}\right). \quad (30)$$

Our experiments, detailed in Section VII, indicate that the Metz and Gaussian filters indeed improve reconstruction quality. Detailed description of the filter equations is given in the Appendix.

VII. Experimental Results

An implementation of the COSEM algorithm described above has has been tailored to the GEMS Millenium-VG tomograph [11]. This scanner consists of two detectors revolving around the FOV. Each of the detectors is of the dimensions 540 $\times$ 400 $\times$ 15.8 mm. The scanner is capable of producing data in limited angle 3-D mode, (with axial lead septas mounted) and in full 3-D mode, (without the led septas). The experiments presented here are based on three studies all acquired in limited 3-D mode. The phantoms are heart and lungs with four inserts and lungs and abdomen with four inserts. The real patient data includes an abdomen study. The limited 3-D mode is mainly used in lungs and abdomen acquisition to limit the bladder emission out of FOV random effects; the maximal axial detection angle is $\pm 8°$. The full 3-D mode allows maximal axial detection angle of $\pm 30°$ and is mainly used for brain studies. The studies are not corrected for attenuation except for phantom 1. The studies properties are given described in Table I. An approximate chart of the two phantoms structures is presented in Fig. 4.

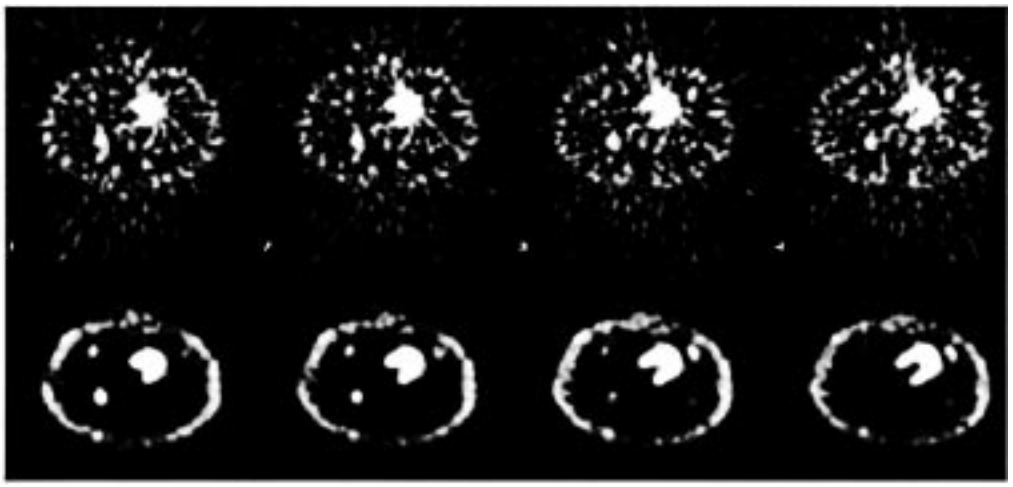

Fig. 5. Four central slices of phantom 1. (top) FBP reconstruction. (bottom) COSEM reconstruction.

TABLE II
FOM COMPARISIONS FOR FIG. 5

FOM	FBP	Pure COSEM	COSEM End filtering	COSEM Iterative Filtering
CR	3.3	4.5	3.9	4.2
CV	0.21	0.4	0.16	0.12

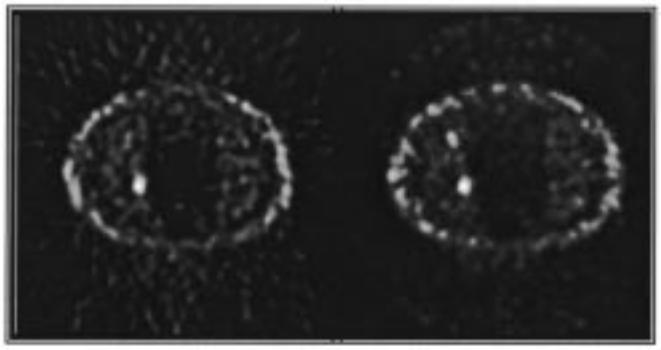

(a) (b)

Fig. 6. Slice 42 of phantom 2. (a) FBP reconstruction. (b) COSEM reconstruction.

TABLE III
FOM COMPARISIONS FOR FIGS. 6 AND 7

Metz	CR	CV
Gaussian	4.2	0.12
Metz P=0.5	4.3	0.12
Metz P=1.0	4.4	0.12
Metz P=1.5	4.7	0.14
Metz P=2.0	4.8	0.25
Metz P=2.5	4.8	0.34

The results of the COSEM reconstruction are compared to that of the filtered backprojection (FBP) algorithm and to COSEM with only postfiltering. Postfiltering was carried out using the same filtering routines as those used in COSEM. FBP reconstructions were made using the commercial software for the GEMS Millenium VG scanner. The FBP reconstructions use the default clinical script of the Millenium VG (Hanning 25/5 filter). Performance was evaluated quantitatively with

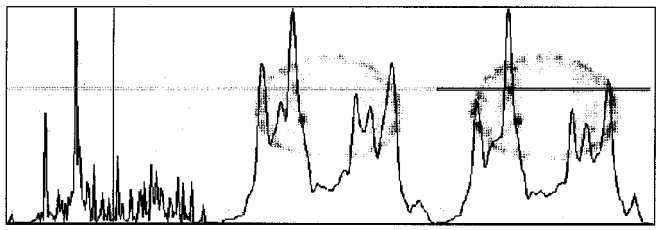

(a) (b) (c)

Fig. 7. Effect of Gaussian filtering on background noise levels. (a) Pure COSEM. (b) Gaussian end filtering. (c) Gaussian filtering every eight subiterations.

TABLE IV
EFFECT OF METZ END FILTERING

FOM	FBP	COSEM+iterative Gaussian
CR	12.1	14.2
CV	0.15	0.09

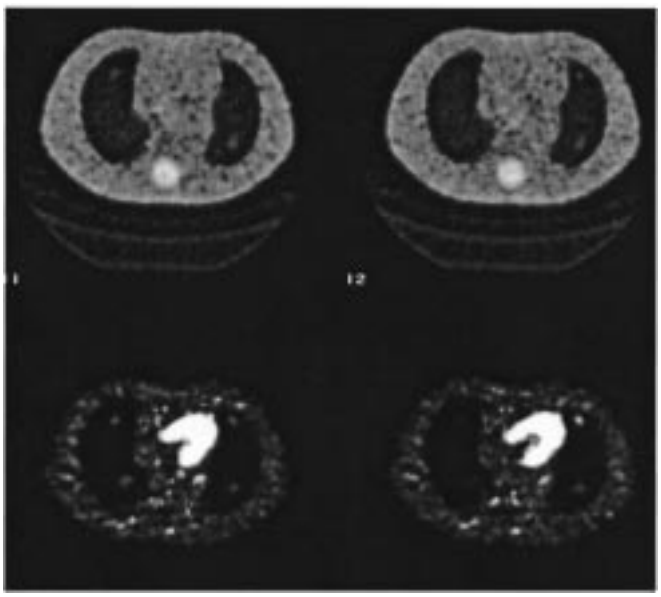

Fig. 8. On-the-fly attenuation correction of Phantom I. (top) Attenuation Maps. (bottom) Attenuation-corrected images of Fig. 7.

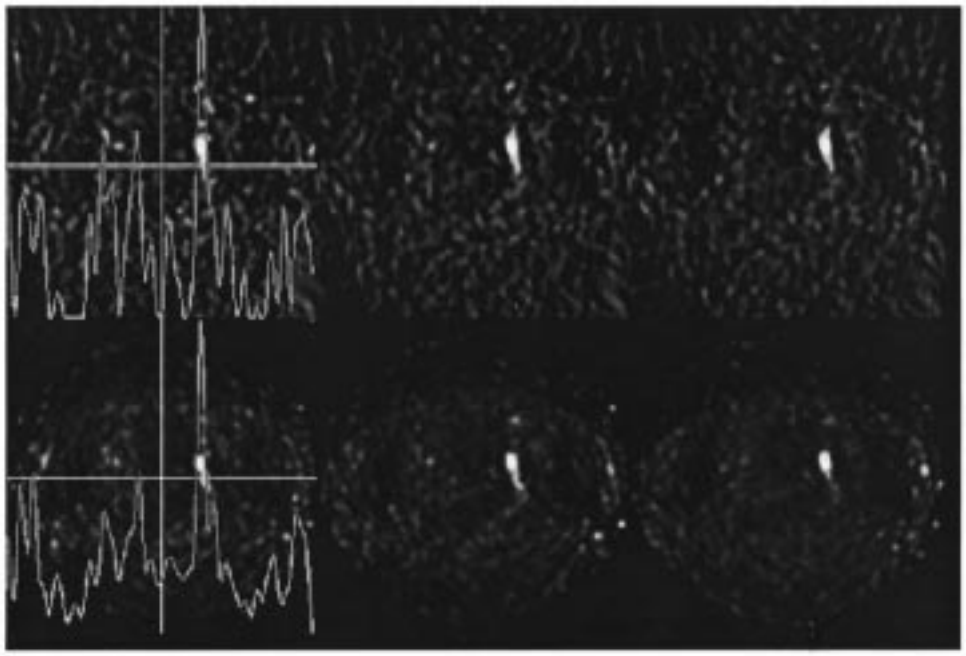

Fig. 9. (top) FBP reconstruction of clinical 1. (bottom) COSEM reconstruction.

respect to two figures of merits (FOM), namely the coefficient of variation (CV) [8] and contrast recovery (CR) [3]. CV is a measure of noise and is defined as the ratio of the standard deviation to the mean of the image over some region of interest (ROI). CR measures differences in reconstructed activity levels. We computed CR between a localized, high-activity (hot) region and a background region as

$$\mathrm{CR} = mean(local)/mean(background)$$

where mean(local) and mean(background) refer to means taken over appropriately placed ROIs. In our analysis, we examined CR and the background CV for hot phantom lesions of different sizes.

The figures presented below contain slices of the reconstructed images. After many trials, COSEM defaults were fixed to four outer iterations, five subsets/iteration with Gaussian filter full-width at half maximum (FWHM) of 8 mm every eight iterations. Image slices presented here are always 4 mm thick.

Fig. 5 shows the results of COSEM reconstruction versus FBP reconstruction on phantom 1 (without attenuation correction on both images). All four inserts are clearly visible in the COSEM reconstruction but only two in FBP reconstruction. The third and forth inserts can be seen but are at same intensity as the noise. The two FOMs were averaged on five ROIs with the results summarized in Table II.

The same differences are also visible in phantom 2 reconstruction in Fig. 6. The 8-mm insert is clearly visible in the COSEM+ Gaussian reconstruction but only hardly distinguishable in FBP. The FOM results are summarized in Table III.

The effect of filtering and iterative filtering is visible in Fig. 7 and in Table III. Fig. 7(a) shows COSEM without any filtering. Although the inserts are statistically distinguishable, the eye can hardly see them due to the image streakiness. Fig. 7(b) uses the data of Fig. 7(a) with filtering. The inserts are visible but the level of noise is increased. The graph of Fig. 7(a) clearly shows that iterative filtering reduces the noise level.

Metz filtering, presented in Table IV for the same image as in Table III, can be used iteratively or only at the end of the reconstruction process. We have found that in the cased of limited statistics, it is better to apply the Metz filter only at the end. In general, increasing the Metz filter power parameter increases the contrast and increasing the FWHM parameter increases smoothness. After many trials the filter with power $= 1.5$ and FWHM 0.8 was chosen as default. Filters with higher power value increase noise and artifacts in the image.

Fig. 8 show the results of running COSEM with the attenuation correction algorithm described in Section III.

Finally, Fig. 9 suggests that specificity, resolution and signal-to-noise ratio are better in COSEM also for a clinical case with very little data. This demonstrates the potential of extending the COSEM algorithm research to the reconstruction of dynamic list-mode data.

VIII. Conclusion

We have presented the design concept and the implementation of the iterative COSEM algorithm. The COSEM is a derivative of the OSEM algorithm, specially adapted to directly process list-mode data from full 3-D acquisition. When applied to a list-mode data acquired from a dual-head rotating tomograph, the COSEM algorithm is likely to produce images with better separation resolution quality and lower noise pattern then than the convolution backprojection algorithms used by the tomograph manufacturer. Exact calculation of the probability matrix and iterative filtering proved to be effective tools for resolution restoration, visual noise reduction, and image quality improvement.

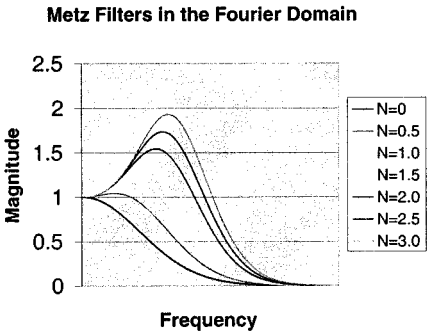

Fig. 10. Metz filters Fourier domain, $N = 0$ is a Gaussian, the middle frequencies are enhanced with the growth of the power parameter.

APPENDIX
METZ FILTERING

The PSF of the system is usually estimated by a 3-D Gaussian function. For convenience, we assume that this Gaussian is spherically symmetric with equal standard deviation (or FWHM) in all directions

$$\text{PSF} \cong Gauss\left(\frac{x^2+y^2+z^2}{2\sigma^2}\right)$$

where σ is the standard deviation

$$\sigma^2 = \frac{(\text{FWHM})^2}{8\ln 2}.$$

Inverse filtering via fast Fourier transform (FFT), used for filtered back projection, is used to deconvolve the Modulation Transfer Function (MTF) from the data in the Fourier space

$$\begin{aligned}\text{MTF} &= \text{FFT}(\text{PSF})\\ \text{Inverse\_Filter}(DATA)&\\ &= \text{FFT}^{-1}\left(\frac{\text{FFT}(DATA)}{\text{MTF}}\right).\end{aligned}$$

The Metz regularization is a truncated power series estimation of the inverse filter kernel (1/MTF). The power series estimation of the inverse filter is

$$\begin{aligned}\frac{1}{\text{MTF}} &= \frac{\text{MTF}^*}{|\text{MTF}|^2} = \frac{\text{MTF}^*}{1-(1-|\text{MTF}|^2)}\\ &= \text{MTF}^* \sum_{m=0}^{\infty}(1-|\text{MTF}|^2)^m.\end{aligned}$$

A Metz filter of order N cuts the series estimation at the power N

$$\begin{aligned}\text{METZ}(N) &= \text{MTF}^* \sum_{m=0}^{N}(1-|\text{MTF}|^2)^m\\ &= \text{MTF}^* \frac{1-(1-|\text{MTF}|^2)^{N+1}}{1-(1-|\text{MTF}|^2)}\\ &= \frac{1-(1-|\text{MTF}|^2)^{N+1}}{\text{MTF}}.\end{aligned}$$

$\text{METZ}(\omega, N, \text{FWHM})$ is defined in the Fourier space.

Note that since $\int \text{PSF} = 1 \Rightarrow \text{MTF}(0) = 1$then the higher N becomes the more the Metz filter approaches inverse filter (see Fig. 10). Similarly, for $N = 0$, the Metz filter is the Gaussian. Therefore, the Metz filter is a controlled band enhancing filter.

ACKNOWLEDGMENT

The authors would like to thank the ELGEMS staff and especially Dr. M. Wilk, Dr. G. Berlad and Dr. Y. Hefetz for their help and insights.

REFERENCES

[1] H. H. Barrett, T. White, and L. C. Parra, "List mode likelihood," *J. Opt. Soc. Amer.*, vol. A 14, pp. 2914–2923.
[2] G. Berlad, D. Falikman, R. Levkovitz, and M. Zibulevski, "An iterative Clist ordered set reconstruction algorithms for 2-D and 3-D coincidence acquisition tomography," Nuclear Medicine Department, Elscint Ltd., Haifa, Israel, Internal Rep., 1996.
[3] M. E. Daube-Witherspoon and J. S. Karp, "Measurement of image quality in 3-D PET," in *Proc. 1999 Int. Meeting Fully Three-Dimensional Image Reconstruction in Radiology and Nuclear Medicine*, 1999, pp. 69–72.
[4] M. Defrise, "Private communication," unpublished.
[5] H. M. Hudson and R. S. Larkin, "Accelerated image reconstruction using ordered subsets of projection data," *IEEE Trans. Med. Imag.*, vol. 13, pp. 601–609, Dec. 1994.
[6] D. Falikman, R. Levkovitz, and Zibulevski, "Penalized COSEM algorithm," Minerva Optimization Centre, Technion and the PARAPET Consortium, Technical report, 1998.
[7] S. R. Meikle, B. F. Hutton, D. L. Bailey, P. K. Hooper, and M. J. Fulham, "Accelerated EM reconstruction in total body PET: Potential for improving tumor delectability," *Phys. Med. Biol.*, vol. 39, pp. 1689–1704, 1994.
[8] *Performance Measurements of Positron Emission Tomographs*, NEMA Standards Pub., NU 2, 1994.
[9] L. A. Shepp and Y. Vardi, "Maximum-likelihood reconstruction for emission tomography," *IEEE Trans. Med. Imag.*, vol. MI-1, pp. 113–122, 1982.
[10] A. J. Reader, K. Erlandsson, M. A. Flower, and R. J. Ott, "Fast accurate iterative reconstruction for low statistics positron volume imaging," *Phys. Med. Biol.*, vol. 43, pp. 835–846, 1998.
[11] The Millenium VG scanner, and the COSEM algorithm, Elgems, Haifa, Israel. [Online]. Available: www.gemedicaldirect.com